AIAA AVIATION Forum
5-9 June 2017, Denver, Colorado
47th AIAA Fluid Dynamics Conference

The effect of sponge layers on global stability analysis of Blasius boundary layer flow

Wei Ran *
University of Southern California, Los Angeles, CA, 90089, USA

Armin Zare†
University of Southern California, Los Angeles, CA 90089, USA

Joseph W. Nichols ‡
University of Minnesota, Minneapolis, MN 55455, USA.

Mihailo R. Jovanović §
University of Southern California, Los Angeles, CA 90089, USA.

In this paper, we conduct a parametric study on the influence of sponge layer strength on temporal eigenvalue problems arising from the one-dimensional wave equation and the linearized Navier-Stokes equations. Sponge layers have shown to stabilize eigenmodes and introduce additional spatial growth to eigenfunctions. As the strength of sponge layers increases, temporal eigenvalues are displaced and the spatial growth rates of their associated eigenfunctions are modified. In both wave and linearized Navier-Stokes equations, the linear relationship between temporal damping and spatial growth can be specified as an approximate dispersion relation. It can also be shown that an over strengthened sponge layer can reflect spatially propagating waves. This reflection can lead to a destabilization of the otherwise stable eigenspectrum with alteration of eigenfunction wavelengths. We provide an empirical guideline for determining the desirable sponge layer strength and demonstrate the efficacy of our method in the global stability analysis of the linearized Navier-Stokes equations.

I. Introduction

The stability analysis of boundary layer flows is crucial to the prediction of laminar-turbulent transition. After the transition of boundary layer flow over an airfoil, skin-friction drag increases significantly. Since extra thrust is required to overcome the increase in drag, transition is considered as a major contributor to airplane fuel expenditure. High-fidelity simulations are able to predict different transition scenarios for a zero-pressure gradient flat-plate boundary layer [1]. However, the computational expense of such simulations prevents their use in fast-turnaround design cycles, thus, predictive reduced-order models are essential in the design process.

Linear stability analysis based on the assumption of locally parallel flow has explained many features of boundary layer transition and provides one such model. The assumption of a locally parallel base flow is rather severe, however, and quickly becomes invalid in the presence of complex geometry [2]. To treat more realistic base flows that vary in the streamwise direction, stability solutions based on the parabolized stability equations have also seen some success [3, 4]. Because such formulations rely on a slowly varying base flow in the streamwise direction, recent efforts have examined boundary layer stability in the context

*Graduate student, Aerospace and Mechanical Engineering, AIAA Student Member.
†Post-doctoral Research Associate, Electrical Engineering, IEEE Member.
‡Assistant Professor, Aerospace Engineering and Mechanics, AIAA Member.
§Professor, Electrical Engineering, IEEE Senior Member

of global mode analysis [5–7]. Since global mode analysis does not rely on the slowly varying nature of the base flow, it can be used to analyze the stability of flows over complex geometries in a natural way.

Due to the convective nonnormality of the flow dynamics [8], however, previous studies have found global modes to be sensitive to the size of the computational domain as well as the streamwise boundary conditions. As an example, figure 1b shows two eigenspectra resulting from global stability analysis of a flat-plate boundary layer with different streamwise boundary conditions. This illustrates how different artificial boundary conditions can result in drastically different eigenspectra, and can even change the stability of the system. Typically, the influence of boundary conditions can be mitigated by applying sponge layers in the streamwise direction of the flow [9, 10].

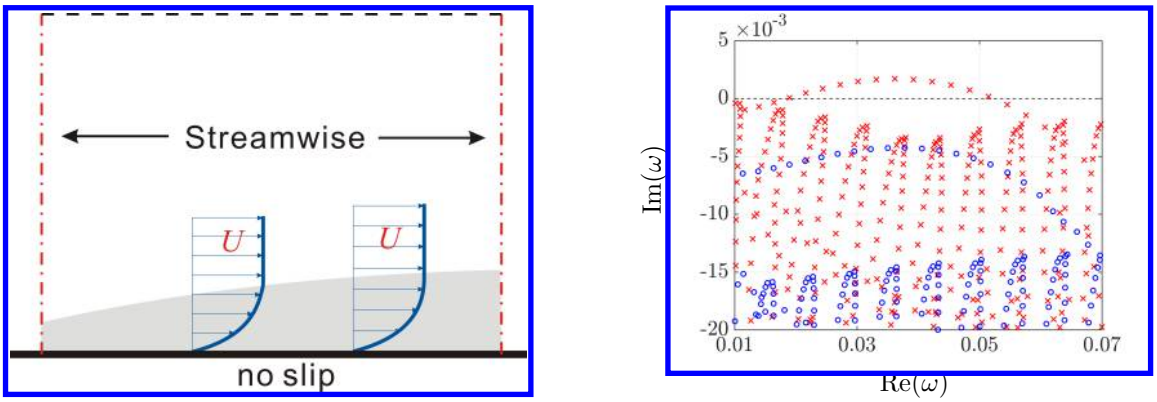

(a) (b)

Figure 1: (a) Truncated computational region (dashed box) for a flat-plate boundary layer. The red dash-dotted line indicates where different boundary conditions are applied. (b) The temporal eigenspectrum of a flat-plate boundary layer flow subject to *Robin-Robin* (×) and *Dirichlet-Extrapolation* (○) boundary conditions. The Dirichlet-Extrapolation boundary conditions result in a stable spectrum.

In this paper, we investigate the sensitivity of global modes of the boundary layer flow in the presence of wave-absorbing sponge layers in the streamwise direction. The paper is organized as follows. In section II, we consider global stability analysis of the wave equations to gain insight into the effect of sponge layers. In section III, we focus on the global stability analysis of the Blasius boundary layer flow with sponge layers to study the effect of sponge layers on temporal eigenvalues and eigenfunctions. In section IV, we verify our observations by solving the infinite-time horizon problem for steady-state velocity covariances in the Blasius boundary layer flow. Finally, we provide concluding thoughts in section V.

II. Wave equation

In this section, we study the eigenvalue problem for the one dimensional linear wave equations. Since the essence of the complex dynamics of boundary layer flows can be captured by the spatial growth (decay) of propagating waves, we use this simple model to gain insight into the influence of sponge layers on the dynamics.

The two-way wave equation can be considered as a coupled system of two first-order equations

$$\begin{aligned} \frac{\partial u}{\partial t} &= -\frac{\partial v}{\partial x} - \sigma(x)\, u \\ \frac{\partial v}{\partial t} &= -\frac{\partial u}{\partial x} - \sigma(x)\, v, \end{aligned} \tag{1}$$

where u and v are the wave functions defined in the domain $x \in [-1,\ 1]$. Homogeneous Dirichlet boundary conditions are imposed for u at both ends of the domain. Without sponge layers, waves striking either end of the domain are perfectly reflected back into the domain. To model open boundaries, however, we include sponge layers represented by the function $\sigma(x)$, which is non-zero only close to the boundaries. When $\sigma(x) > 0$, waves are gradually driven back to zero.

To form the temporal eigenvalue problem, the wave functions are expressed in wave form as $u(x,t) = \hat{u}(x)\exp(-\mathrm{i}\omega t)$ and $v(x,t) = \hat{v}(x)\exp(-\mathrm{i}\omega t)$. This yields the eigenvalue problem

$$
\begin{aligned}
-i\,\omega\,\hat{u} &= -\frac{\partial \hat{v}}{\partial x} - \sigma(x)\,\hat{u} \\
-i\,\omega\,\hat{v} &= -\frac{\partial \hat{u}}{\partial x} - \sigma(x)\,\hat{v}.
\end{aligned}
$$

When the sponge layer is not applied ($\sigma(x) = 0$), eigenvalues and corresponding eigenfunctions can be analytically derived as $\omega = n\pi/2$ ($n \in \mathbb{Z}$), $\hat{u} = \sin(\omega x)$ and $\hat{v} = -\mathrm{i}\cos(\omega x)$, respectively.

Parabolic shaped sponge layers are placed at both ends of the computational domain. The thickness of each sponge layer is $L_s = 0.1225$ ($\sigma(x) = 0, x \in [-0.8775,\ 0.8775]$). The strength of the sponge layer is defined as $S_s := \sigma(\pm 1)$. Chebyshev polynomials are adopted to discretize the computational domain with 200 collocation points. We study 20000 cases of sponge layer strengths growing linearly from 1 to 10^6.

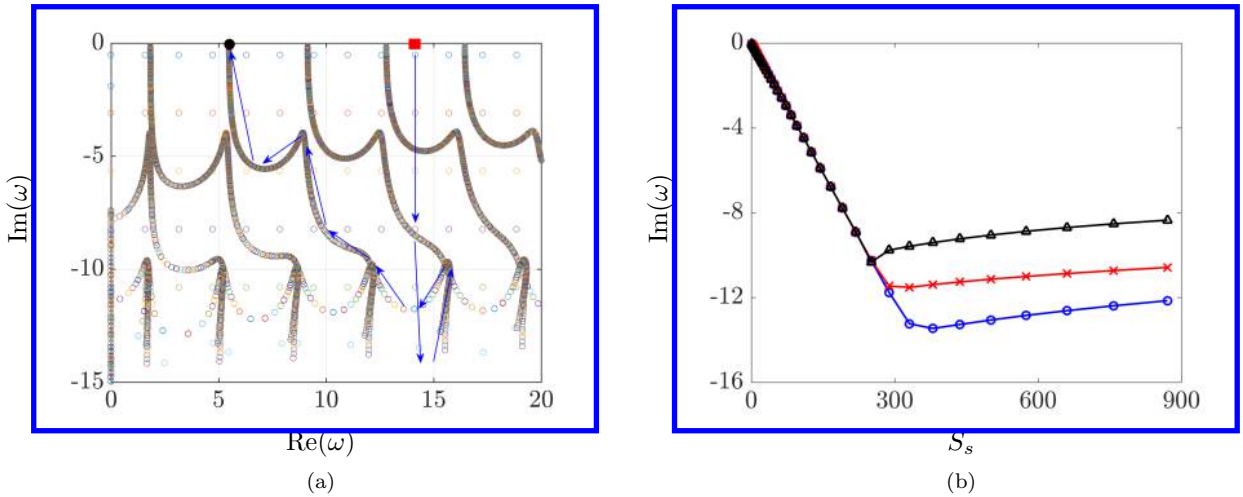

(a) (b)

Figure 2: Displacement of eigenvalues as the sponge layer strength increases; (a) the displacement trajectories of eigenvalues start from $\omega_0 = 9\pi/2$ ($S_s = 0$, red square) and end at $\omega = 5.2923 - 0.1114i$ ($S_s = 10^6$, black dot); (b) Imaginary parts of eigenvalues from three different trajectories starting at $\omega_0 = \pi/2$ ($\circ$), 10π ($\times$), and 50π ($\triangle$) as a function of sponge layer strength.

Figure 2a shows the trajectories of eigenvalues. Blue arrows show the approximate path of eigenvalues starting from $\omega_0 = 9\pi/2$ due to the increase in the sponge layer strength. Other eigenvalues in the spectrum follow similar trajectories. Starting from the real axis, the eigenvalues move down, but eventually turn around after the sponge strength exceeds a certain value. In the limit of $S_s \to \infty$, the eigenvalues move back to a shifted position on the real axis; see black dot at the end of the trajectory in figure 2a. Figure 2b shows how the imaginary part of various eigenvalues can change as a function of sponge layer strength. After an initial decrease in the imaginary part of these eigenvalues we observe a *turn-around* behavior followed by an increase happening beyond a critical sponge layer strength of $S_s \approx 300$.

The increase in $\mathrm{Im}(\omega)$ is caused by a reflection of waves from the sponge layer. The damping rate of waves passing though the sponge layer is proportional to $\exp(-2\int_0^{L_s}\sigma(x)\,dx)$ [10]. This implies that stronger sponge layers better absorb waves. However, it is also observed that significantly strong sponge layer can cause wave reflection [10]. This is a similar phenomenon to the echo of sound (waves) when they hit a solid wall, or an infinitely strong sponge layer. As shown in figure 3, in the extreme case ($S_s = 10^6$), the eigenfunction retains its sinusoidal shape, but with a different wavelength. Figure 3b shows that infinitely strong sponge layers form new boundaries with homogeneous Dirichlet boundary conditions, ultimately shrinking the computational domain. We thus infer that strong sponge layers can shrink the domain and detune eigenfunctions.

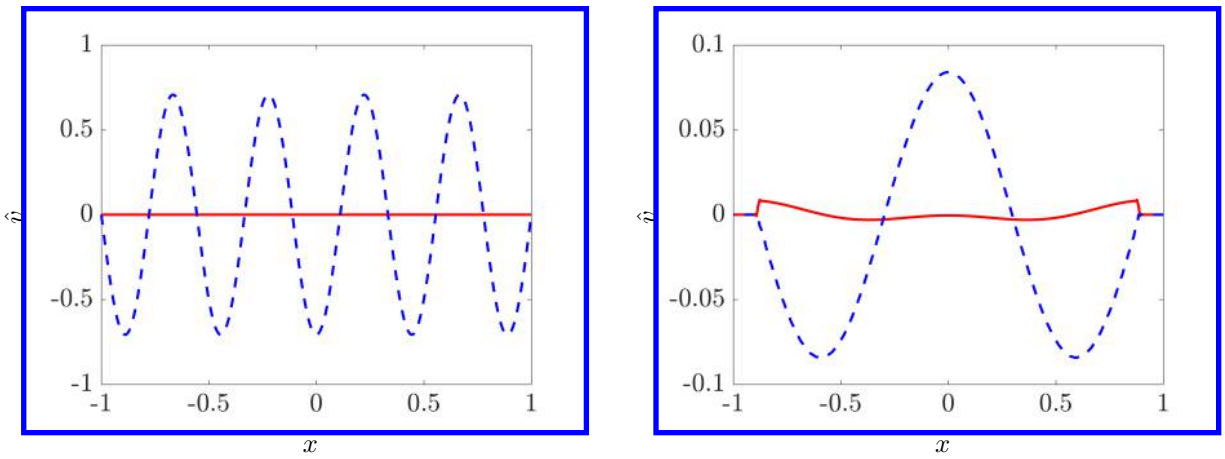

(a) (b)

Figure 3: Real (dashed) and imaginary (solid) parts of the eigenfunction $\hat{v}$ corresponding to the trajectory originating at $\omega_0 = 9\pi/2$ with (a) no sponge layer ($S_s = 0$), and with (b) a sponge layer of strength $S_s = 10^6$.

Figure 4 shows the amplitude of two eigenfunctions from the trajectory that starts at $\omega_0 = 10\pi$. Even though the wave equation provides no instability mechanism, figures 4a and 4b show that the eigenfunctions experience significant spatial growth. This growth is required for each crest to maintain constant amplitude as it propagates away from the center of the domain, even though the entire mode is damped in time. Figures 4c and 4d illustrate the exponential spatial growth in the amplitude of $\hat{v}$. In the exponential growth region, the amplitude of the wave perfectly collapses on lines denoting a $|\mathrm{Im}(\omega)|$ growth-rate for upstream and downstream traveling waves. To explain this, without loss of generality, we only consider the right propagating waves. The solution to the wave equation can be formed as $\exp(\mathrm{i}kx) \times \exp(-\mathrm{i}\omega t) + c.c.$, where k is the complex wavenumber and ω is the eigenvalue. The phase speed of traveling waves is 1 in the non-sponged domain with no dispersion, i.e., $\omega/k = c = 1$, and as a result $k = \omega$. As a consequence the spatial growth rate $-\mathrm{Im}(k)$ is the negative of the temporal damping rate $\mathrm{Im}(\omega)$, i.e., $-\mathrm{Im}(k) = -\mathrm{Im}(\omega)$. Moreover, the spatial wavenumber $\mathrm{Re}(k)$ is equal to temporal frequency $\mathrm{Re}(\omega)$. As a result, the nontrivial shift in the real part of the eigenvalues $\mathrm{Re}(\omega)$ entails a shift in $\mathrm{Re}(k)$, which can be related to the reflecting property of the sponge layer. While figure 4c shows a smooth decay of $|\hat{v}|$ within the sponge region, figure 4d shows that a strong sponge layer can result in significant oscillations. We relate such oscillations to the reflection of waves from sponge layers.

III. Global stability analysis of the Blasius boundary layer

The lack of streamwise homogeneity significantly complicates the dynamics of spatially evolving flows. In this section, we consider the global stability analysis of temporal eigenvalues in the Blasius boundary layer flow. The Reynolds number $Re = U_\infty \delta_0/\nu$ based on the free stream velocity $U_\infty = 1$ and the boundary layer thickness at the inlet $\delta_0 = \delta(0)$ is 400. The Navier-Stokes (NS) equations are linearized around the Blasius velocity profile $[\,U(x,y)\;\; V(x,y)\,]^T$, which yields the governing equations for fluctuations in velocity $[\,u\;\; v\,]^T$ and pressure p. Assuming wavelike solutions, $u(x,y,t) = \hat{u}(x,y)\exp(-\mathrm{i}\omega t)$, we arrive at the temporal eigenvalue problem

$$\begin{aligned} -\mathrm{i}\,\omega\,\hat{u} &= \left(C - \frac{\partial U}{\partial x}\right)\hat{u} - \frac{\partial U}{\partial y}\,\hat{v} - \frac{\partial \hat{p}}{\partial x} - \sigma(x)\,\hat{u} \\ -\mathrm{i}\,\omega\,\hat{v} &= \left(C - \frac{\partial V}{\partial y}\right)\hat{v} - \frac{\partial V}{\partial x}\,\hat{u} - \frac{\partial \hat{p}}{\partial y} - \sigma(x)\,\hat{v} \\ 0 &= \frac{\partial \hat{u}}{\partial x} + \frac{\partial \hat{v}}{\partial y}, \end{aligned} \tag{2}$$

where $C = \Delta/Re - U\partial/\partial x - V\partial/\partial y$ and $\Delta = \partial^2/\partial x^2 + \partial^2/\partial y^2$.

We consider a computational domain of $L_x = 900\delta_0$ and $L_y = 35\delta_0$. We employ a pseudospectral

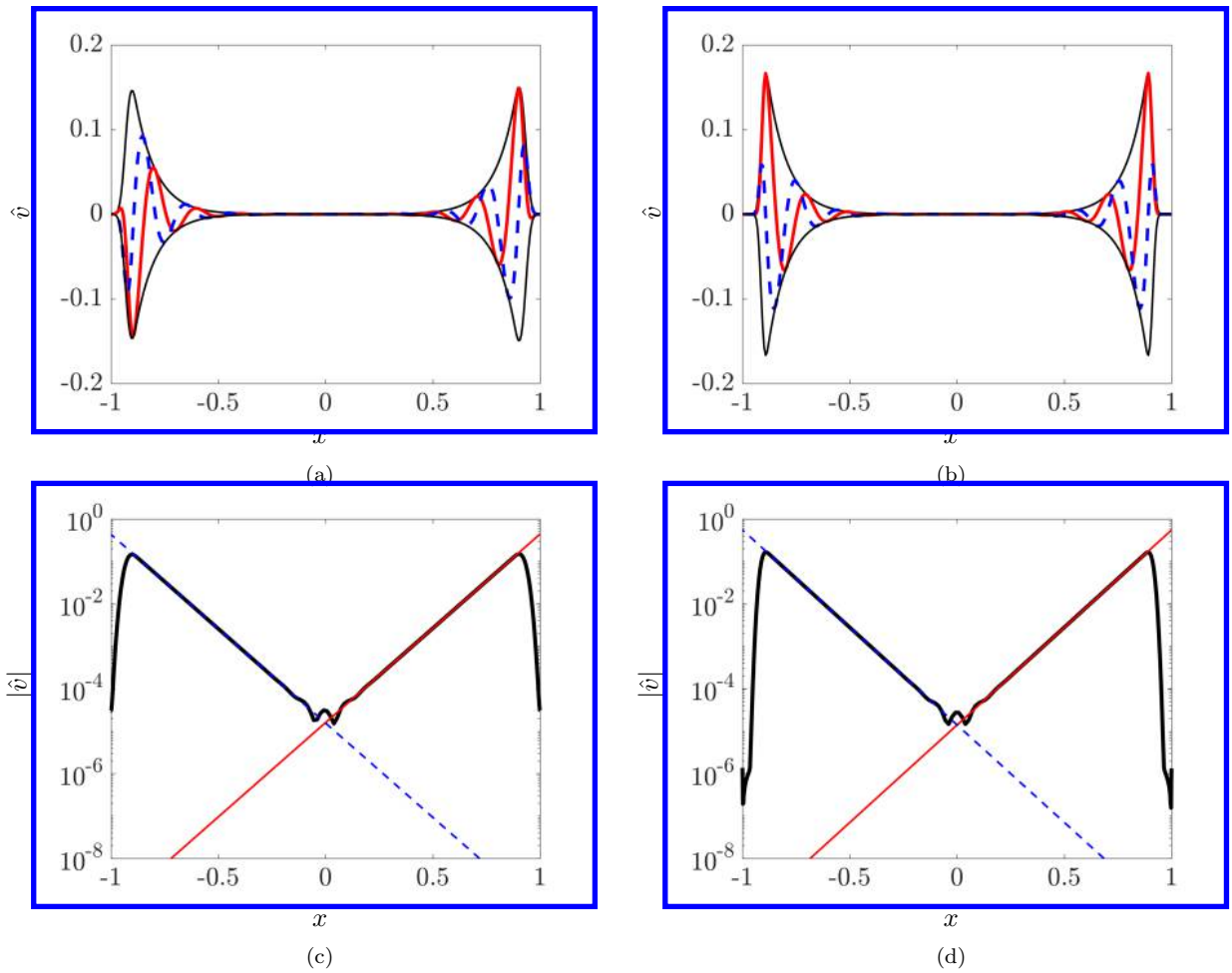

Figure 4: Eigenfunctions $\hat{v}$ from the trajectory starting at $\omega_0 = 10\pi$; left column is at $\omega = 31.4126 - 10.2352i$ with $S_s = 251$ and right column is at $\omega = 32.3432 - 10.5801i$ with $S_s = 871$. (a, b) Envelopes (thin black lines), real (red thick lines) and imaginary (thick blue dashed lines) parts of eigenfunctions. (c, d) Amplitudes of eigenfunctions (thick black lines) and the estimated amplitudes of downstream (thin red lines) and upstream (thin blue dashed lines) propagating eigenfunctions, which are respectively obtained as $|\hat{v}(0.5)| \exp(-\omega_{\rm i}(x - 0.5))$ and $|\hat{v}(-0.5)| \exp(\omega_{\rm i}(x + 0.5))$. Here, $\omega_{\rm i}$ is the imaginary part of ω.

scheme with $N_x = 200$ and $N_y = 50$ Chebyshev collocation points in the streamwise (x) and wall-normal (y) directions, respectively [11]. Homogeneous Dirichlet boundary conditions for velocity fluctuations are applied at the inflow ($x = 0$) as well as the wall ($y = 0$) and in the free-stream ($y = 35\delta_0$). Linear extrapolation is employed as the boundary condition at the outflow ($x = 900\delta_0$) [12],

$$\hat{v}(N_x, y) \;=\; a_1\,\hat{v}(N_x - 1, y) \;+\; a_2\,\hat{v}(N_x - 2, y)$$

$$\hat{u}(N_x, y) \;=\; a_1\,\hat{u}(N_x - 1, y) \;+\; a_2\,\hat{u}(N_x - 2, y)$$

$$a_1 \;=\; \frac{x(N_x) - x(N_x - 2)}{x(N_x - 1) - x(N_x - 2)}, \qquad a_2 \;=\; \frac{x(N_x - 1) - x(N_x)}{x(N_x - 1) - x(N_x - 2)}.$$

We adopt the similar sponge layer shape as in section II; parabolas at both ends of x with a thickness of $L_s = 55$, i.e., $\sigma(x) = 0$ for $x \in [55, 845]$ (cf. Eq. (1)), and solve 50 temporal eigenvalue problems with different sponge layer strengths growing exponentially from 10^{-2} to $10^{0.8}$. We employ the shift and invert technique for solving Eq. (2), which is a common strategy for solving large-scale generalized eigenvalue problems [5, 12–14].

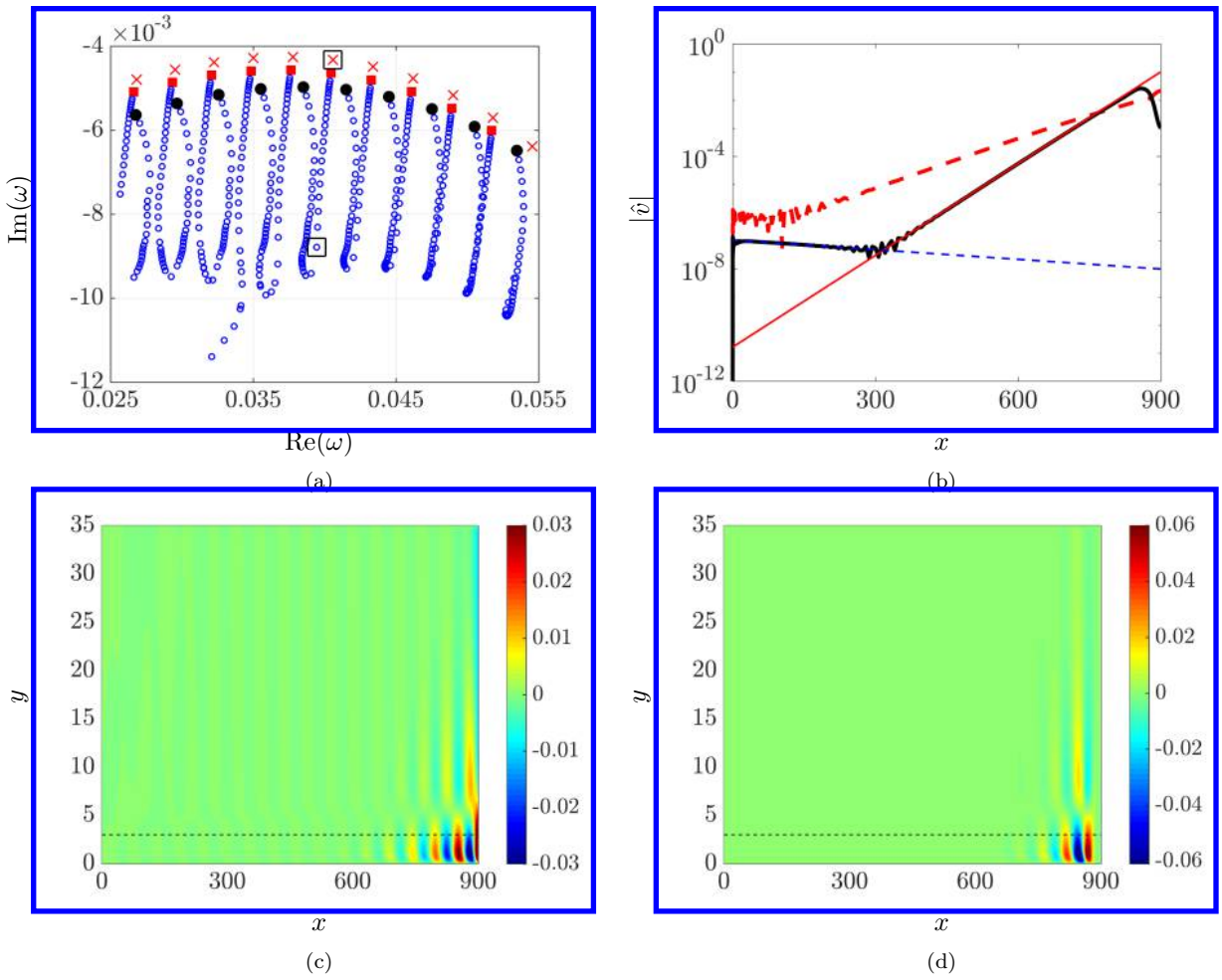

Figure 5: (a) Eigenspectra of TS modes are displaced as the sponge layer strength increases: The red crosses (×) denote the spectrum obtained without a sponge layer ($S_s = 0$); Red squares represent the starting points on the trajectories ($S_s = 10^{-2}$); black dots are the final points on the trajectories ($S_s = 10^{0.8}$); the two black boxes (□) represent the non-sponged and desirablely sponged cases selected for studying the properties of eigenfunctions. (b) Amplitude of two wall-normal velocity component $\hat{v}$ from the non-sponged case ($S_s = 0$, thick red dashed line) with corresponding eigenvalue $\omega = 0.04058 - 0.004325i$ and desirablely sponged case ($S_s = 0.235$, thick black line) with corresponding eigenvalue $\omega = 0.03944 - 0.008787i$. (c) The real part of the streamwise velocity component $\hat{u}$ from the eigenfunction of the non-sponged problem; the amplitude data in (b) is extracted from the black dashed line ($y = 3\delta_0$). (d) The real part of $\hat{u}$ from the eigenfunction of the desirablely sponged case.

Figure 5a shows the temporal eigenspectra of Eq. (2) with different sponge layer strengths. The eigenfunctions of these modes correspond to Tollmien-Schlichting (TS) waves. Similar to section II, the displacement trajectories can be considered as starting at red squares and ending at black dots. Similar to figure 2a, a *turn-around* phenomenon can also be observed, which is an indicator of significant reflection from the sponge layer. As for the wave equation, an desirable sponge layer strength can be determined. We consider the desirable sponge strength as the strength that corresponds to the *turn-around* point beyond which reflection becomes significant. This value is $S_s \approx 0.235$ for the problem considered in this section.

In figure 5a, two modes (on the same trajectory), which are marked with black squares, are selected for further investigation: the upper eigenvalue $\omega = 0.04058 - 0.004325$i corresponds to $S_s = 0$ and the lower eigenvalue $\omega = 0.03944 - 0.008787$i corresponds to the desirablely-sponged case with $S_s = 0.235$. Figures 5c and 5d show the real parts of the streamwise velocity component $\hat{u}$ of the eigenfunctions for the non-sponged and desirablely sponged boundary conditions. Both show significant spatially evolving TS waves. The spatial

growth of the TS wave for the desirablely sponged problem is more pronounced. This demonstrates the effect of the sponge layer and is in harmony with the observations made for the wave equation.

To determine the spatial growth of the selected modes, we consider the amplitude of the wall-normal velocity component $\hat{v}$ at the wall-normal location $y = 3\delta_0$ marked by black dashed lines in figures 5c and 5d. In figure 5b, the amplitude of the mode corresponding to the non-sponged problem is denoted by the thick red dashed line. Its growth in the streamwise direction is almost exponential. The oscillations in the vicinity of the inlet are a result of numerical error. The black solid line in figure 5b corresponds to the desirablely sponged mode with $S_s = 0.235$. For this case, a branch of significant upstream propagating waves is observed close to the inlet. Unlike the wave equation results, however, the spatial growth rates of downstream and upstream propagating waves are different. This is because the phase speeds of downstream and upstream propagating waves are different. On the other hand, the spatial growth rate of the downstream branch from the desirablely sponged mode is significantly larger than that of the non-sponged mode. The weak upstream propagating waves experience very slow growth, which is negligible. Thus, only the downstream propagating branches are considered in the later analyses.

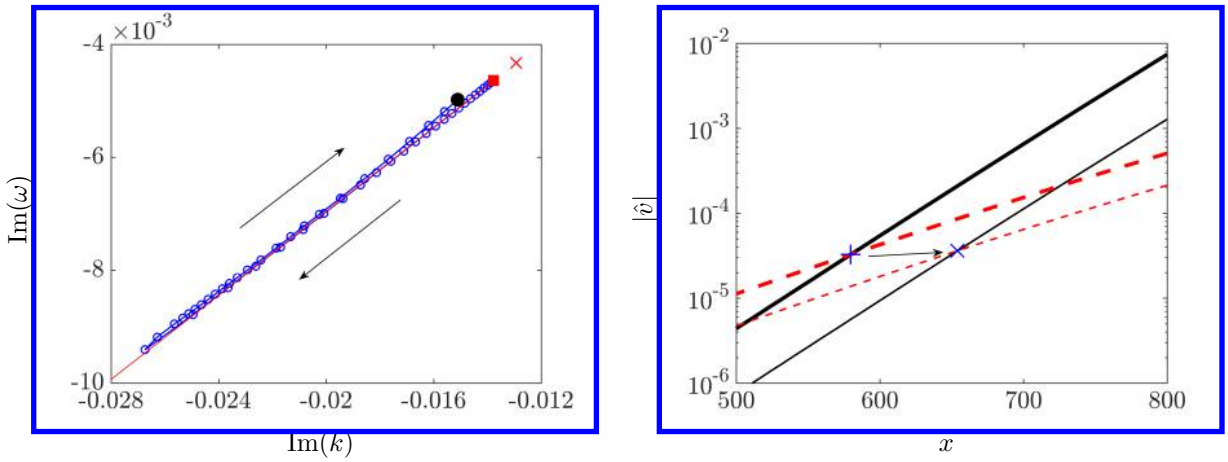

(a) (b)

Figure 6: (a) Relationship between the imaginary part of eigenvalues ω ($\circ$) and the imaginary part of the wavenumber α for the downstream propagating wave when the sponge layer strength grows from 10^{-2} to $10^{0.8}$. The red square denotes the beginning of the trajectory and the black dot denotes the end. The non-sponged case is marked by the red cross ($\times$). The red line is the fitted linear relationship. (b) Evolution of amplitudes of non-sponged and desirablely sponged modes: non-sponged mode at $t = 0$ (thick red dashed line); desirablely sponged mode at $t = 0$ (thick black line); non-sponged mode at $t = 200$ (thin red dashed line); desirablely sponged mode at $t = 200$ (thin black line).

As we observed in the previous section, sponge layers can suppress the temporal growth of eigenfunctions while amplifying their spatial growth. This hints at a relationship between temporal and spatial growth rates. However, since the dispersion relation is more complicated here, the relationship is not as obvious as in the wave equation. To identify this relationship, the eigenfunctions are approximated with the wave packet form: the phase function is $\exp(\mathrm{i}(\alpha x - \omega t))$, where $\mathrm{Im}(\omega)$ is the temporal damping rate and $-\mathrm{Im}(\alpha)$ is the spatial growth rate of eigenfunctions. This is a reasonable approximation because the temporal frequency $\mathrm{Re}(\omega)$ and spatial wavenumber $\mathrm{Re}(\alpha)$ of eigenfunctions from the same displacement trajectory are approximately equal, and the amplitude of eigenfunctions grow exponentially in the streamwise direction. Using this approximation, we can extract $\mathrm{Im}(\alpha)$ from the amplitude of each eigenfunction via linear fitting and as the slope of the red line in figure 5b.

Figure 6a shows the relation between $\mathrm{Im}(\omega)$ and $\mathrm{Im}(\alpha)$ for all eigenvalues on a single trajectory. We obtain an almost perfect linear mapping between the temporal damping rate and the spatial growth rate as

$$\mathrm{Im}(\omega) \;=\; 0.372\,\mathrm{Im}(\alpha) \;+\; 0.000475, \tag{3}$$

which holds even after the *turn-around* phenomenon. The relationship is likely to show the dispersion relation since the slope 0.372 is close to the phase velocity of TS waves which is typically $0.3 \sim 0.4$. To

verify this, the two eigenfunctions considered in figure 5b are adopted again. For visual convenience, we decrease the amplitude of the eigenfunction corresponding to the non-sponged problem by a factor of 10. The eigenfunctions are then evolved from $t = 0$ to $t = 200$. Figure 6b shows the amplitude of the wall-normal component of the eigenfunctions at $t = 0$ and $t = 200$. As shown in this figure, the amplitude of eigenfunctions for both non-sponged and desirablely sponged cases decreases. On the other hand, this decrease in time can be viewed as the propagation of a wave packet in space. Since the phase speed of a wave does not change in the domain with no sponge layers, we choose the point of crossing of red and black lines as two points of interest with the first located at $x = 579.7$ (+) and the second at $x = 654.2$ (×). The wall-normal amplitude of the mode is 3.27×10^{-5} at $x = 579.7$ and is 3.61×10^{-5} at $x = 654.2$. Based on this, a phase speed can be computed for the two eigenfunctions as $c = 0.3725$. This value is equivalent to the slope identified for the in Eq. (3) from figure 6a.

The offset in the linear relation (3) denotes a factor of 1.104 increase in the amplitude of the wave. From the phase function $\exp(\mathrm{i}(\alpha x - \omega t))$, the convective amplitude growth can be computed as $\exp(-\alpha_\mathrm{i}\Delta x + \omega_\mathrm{i}\Delta t)$, where α_i and ω_i denote the imaginary parts of α and ω. From linear relation (3) and $\Delta x = c\Delta t$ we arrive at an amplitude growth of $\exp(0.001279\Delta x)$. This results in a factor of 1.0997 amplitude growth after $\Delta x = 74.5$ (the distance between two points of interest on figure 6b. This is in agreement with the actual growth of 1.104. We can thus write the linear relationship between $\mathrm{Im}(\omega)$ and $\mathrm{Im}(\alpha)$ as:

$$\mathrm{Im}(\omega) \;=\; c\,\mathrm{Im}(\alpha) \;+\; c_0,$$

where c is the phase speed and c_0 is the convective spatial growth rate. For the wave equation, the phase speed is 1 and the convective spatial growth rate is 0, which satisfy this relationship. In fact, if the spatial eigenproblem of the Orr-Sommerfeld equation at $x = 579.7$ ($Re = 626$) is solved using the eigenvalue ω from the global stability analysis in figure 6a, the approximate linear dispersion relation is obtained as

$$\mathrm{Im}(\omega) \;=\; 0.3707\,\mathrm{Im}(\alpha) \;+\; 0.000458,$$

which is very close to the linear relationship we obtained above.

IV. Stochastically-forced linearized NS equations

The flat-plate boundary layer flow, e.g., the Blasius boundary layer flow, is globally stable, i.e., all eigenvalues of the dynamic generator matrix are in the stable half-plane [15]. This allows us to study the long-term response of velocity fluctuations to continuous input disturbances using the steady-state Lyapunov equation corresponding to the linearized NS equations. However, the discretized operators in the linearized NS equations are ill-conditioned and unstable non-physical modes often appear, which limits the utility of the Lyapunov framework. Herein, we build on the insight gained in previous sections to design *desirable* sponge layers that can stabilize such non-physical modes.

The NS equations are linearized around the Blasius boundary layer profile $[\,U(x,y)\;\;V(x,y)\;\;0\,]^T$. We use a similar computational region (L_x, L_y) and free stream velocity (U_∞) as in section III. The Reynolds number is also definied in a similar manner. We bring the linearized equations into its evolution form [16] with state $\boldsymbol{\psi} = [v,\;\eta]^T$. Here, v and η denote wall-normal velocity and vorticity, respectively. We leverage spatial homogeneity in the spanwise direction and apply Fourier transform to the governing equations. The state can thus be expressed as $\boldsymbol{\psi} = \hat{\boldsymbol{\psi}}(x,y,t)\exp(\mathrm{i}\beta z)$, where β is the spanwise wavenumber and $\hat{\boldsymbol{\psi}} = [\hat{v},\;\hat{\eta}]^T$. This brings the linearized NS equations into the following form:

$$\begin{bmatrix} \dot{\hat{v}} \\ \dot{\hat{\eta}} \end{bmatrix} \;=\; \underbrace{\begin{bmatrix} A_{11} & A_{12} \\ A_{21} & A_{22} \end{bmatrix}}_{A} \begin{bmatrix} \hat{v} \\ \hat{\eta} \end{bmatrix} + \underbrace{\begin{bmatrix} B_{11} & 0 \\ 0 & B_{22} \end{bmatrix}}_{B} \begin{bmatrix} d_v \\ d_\eta \end{bmatrix} \tag{4}$$

$$\begin{bmatrix} \hat{u} \\ \hat{v} \\ \hat{w} \end{bmatrix} \;=\; \underbrace{\begin{bmatrix} C_{11} & C_{12} \\ 1 & 0 \\ C_{31} & C_{32} \end{bmatrix}}_{C} \begin{bmatrix} \hat{v} \\ \hat{\eta} \end{bmatrix} \tag{5}$$

The definition of operators A, B and C is provided in the appendix. Here, $[\dot{\hat{v}},\;\dot{\hat{\eta}}]^T$ denotes the time derivative of the state and $\mathbf{d} = [d_v,\;d_\eta]^T$ represent the input forcing corresponding to the dynamics of v and η. We

use a similar pseudospectral scheme as in section III to discretize the operators in the streamwise and wall-normal directions using $N_x = 101$ and $N_y = 50$ collocation points in x and y, respectively. Configuration of boundary conditions and sponge layers follow section III.

When the dynamic generator A is stable, the steady-state covariance of the state $\boldsymbol{\psi}$

$$X \;=\; \lim_{t\to\infty} \left\langle \hat{\boldsymbol{\psi}}(t)\, \hat{\boldsymbol{\psi}}^*(t) \right\rangle,$$

can be obtained as the solution to the algebraic Lyapunov equation

$$A\,X \;+\; X\,A^* \;=\; -\,B\,\Omega B^* \tag{6}$$

where $\langle\cdot\rangle$ is the expectation operator, $*$ denotes the adjoints of operators A and B, Ω is the covariance of zero mean white-in-time stochastic forcing

$$\langle \mathbf{d}(t_1)\mathbf{d}^*(t_2)\rangle \;=\; \Omega\,\delta(t_1 - t_2).$$

For simplicity, we consider $\Omega = I$. The operator B specifies the wall-normal region in which the forcing enters. In this section, we restrict the forcing to a region in the vicinity of the wall (from $y = 0$ to $y = 5\delta_0$) [17]; see the appendix for details. The covariance of velocity fluctuations can be obtained from X as $\Phi = CXC^*$. The steady-state flow structures in the boundary layer flow can be extracted from eigenfunctions of the matrix Φ. The corresponding eigenvalues represent the energy of flow structures [16, 18].

The temporal eigenspectrum for the linearized NS equations with $\beta = 0.01$ is shown in figure 7a. Due to the presence of unstable (non-physical) modes in the upper left region of the spectrum, it is essential to design sponge layers that can stabilize the spectrum and at the same time have minimal effect on the physics of relevant modes. Figure 7b shows the displacement trajectory of eigenvalues that correspond to TS modes. The location corresponding to the desirable sponge layer strength is marked by the black squares (sponge layer strength $S_s = 0.2$), and provides the largest temporal decay. Application of the *desirable* sponge layer stabilizes the eigenspectrum and sufficiently suppresses the non-physical modes; see figure 7a. In contrast, the eigenvalues corresponding to the TS modes are less decayed.

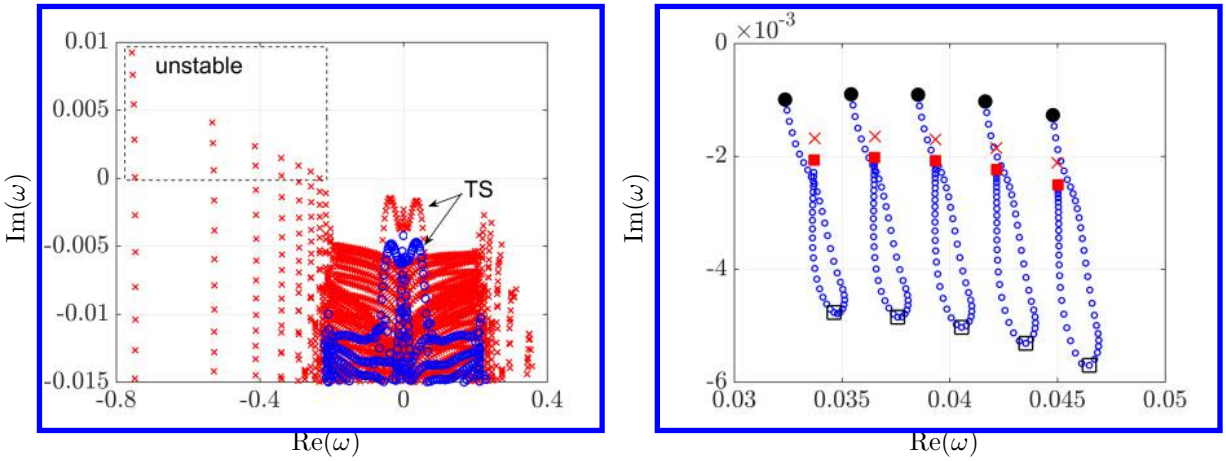

(a) (b)

Figure 7: (a) The temporal eigenspectrum of the linearized NS equations with no sponge layer ($\times$), and with the desirablely strengthened sponge layer $S_s = 0.2$ ($\circ$). (b) The displacement of the eigenvalues corresponding to the TS modes as the sponge layer strength increases; the spectrums without the sponge layer ($\times$), red squares show the beginning of trajectories ($S_s = 10^{-2}$), black dots are the final points on the trajectories ($S_s = 10^{0.8}$). The black boxes ($\square$) represent the desirablely sponged case ($S_s = 0.2$).

Figure 8 shows the real part of the streamwise velocity component of the principle and second most energetic modes of Φ. The covariance matrix Φ results from solving the Lyapunov equation in the presence of sponge layers with strength $S_s = 0.2$. The physical structure of these modes is similar to TS waves

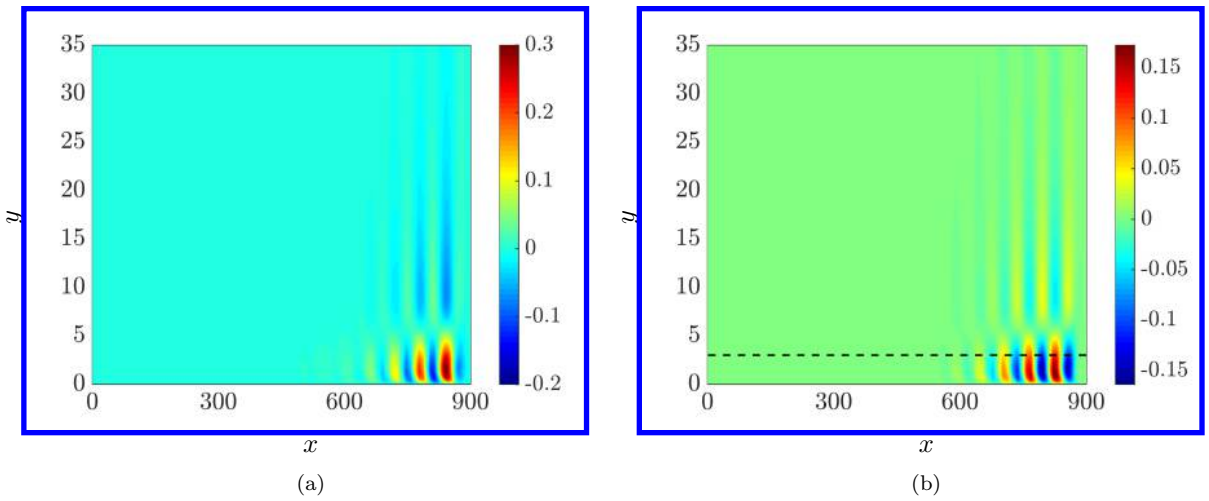

(a) (b)

Figure 8: Flow structures (real part of streamwise velocity fluctuation) extracted from the eigenvalue decomposition of the covariance matrix Φ; (a) the principle (most energetic) mode, (b) the second mode.

extracted from the corresponding dynamic generator A. Due to this visual similarity, one may conclude that they are resonant forms of multiple TS waves excited by white stochastic forcing. However, this remains to be proven.

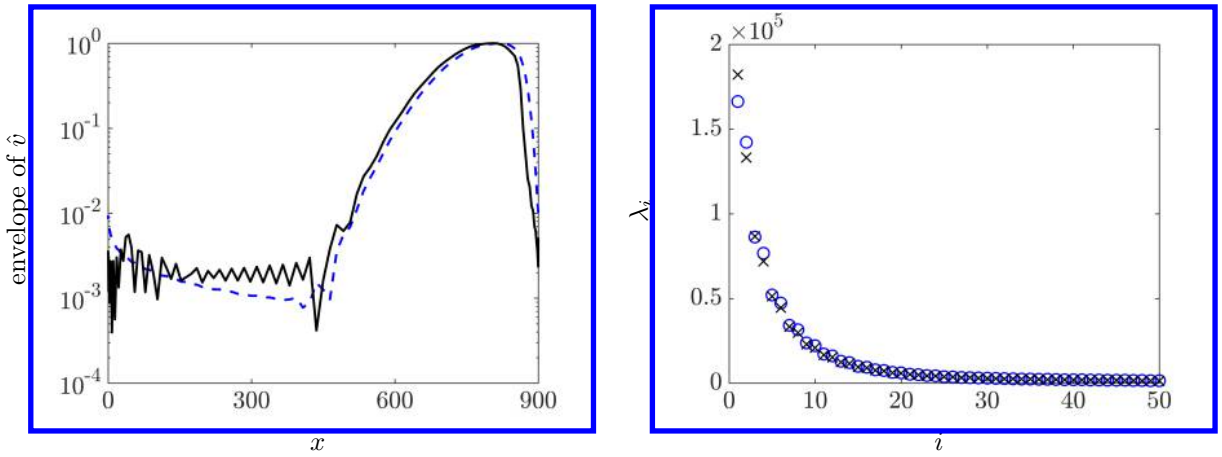

(a) (b)

Figure 9: (a) The envelope of $\hat{v}$ at $y = 3\delta_0$ extracted from the second most significant mode of Φ with a sponge layer strength of $S_s = 0.2$ (dashed line) and $S_s = 4$ (solid line). (b) The first 50 eigenvalues of Φ with a sponge layer strength of $S_s = 0.2$ ($\circ$) and $S_s = 4$ ($\times$).

We next investigate the influence of different sponge strengths ($S_s = 0.2,\ 4$) on the steady-state response. Figure 9a shows the normalized envelope of the wall-normal component of the second eigenfunction of Φ at $y = 3$ as a function of x. This figure shows that the strength of the sponge layer has minimal influence on the envelope of the second mode. Our observations show that unlike the eigenfunctions studied in section III, no additional spatial growth is introduced by the sponge layers. In addition, as shown in figure 9b, the first 50 eigenvalues of the covariance matrix Φ do not significantly change due to different sponge layer strengths. Figure 9a also shows the effect of a strong sponge layer in shrinking the computational domain in the streamwise direction, as well as inducing wave reflections into the solution. As shown in figure 9b, when the sponge layer strength increases, the energy of the principle mode increases whereas the energy of the second mode decreases. As a result, the total energy ($\sum \lambda_i$) is kept approximately intact. This shows the ability of the sponge layer in affecting the receptivity of individual modes to exogenous disturbances.

V. Conclusion

In the present study, we have investigated the effect of sponge layers on the global stability analysis of the two-way wave equation and the linearized Navier-Stokes equations. Sponge layers can cause temporal damping of eigenmodes, and at the same time, introduce additional spatial growth to eigenfunctions. They can also induce the reflection of waves. For temporal eigenvalue problems derived from wave and linearized Navier-Stokes equations, the eigenspectra are displaced as the sponge layer strength increases. In particular, we have identified a turn-around behavior in the displacement trajectories of eigenmodes that allowes us to determine the desirable strength of sponge layers in these problems. In addition, we have deduced the relationship between the temporal damping rate and spatial growth rate of eigenmodes. In the future, we will investigate the effect of other parameters, e.g., width and shape of sponge layers in the global stability analysis of spatially evolving flows. We have recently employed our findings to compute the desirable strength of sponge layers in the global analysis of stochastically forced linearized NS equations [19].

Appendix

We show the operators in Eq. (4):

$$
\begin{aligned}
A_{11} &= \Delta^{-1}\left[\frac{1}{Re}\Delta^2 - U\Delta\frac{\partial}{\partial x} - V\Delta\frac{\partial}{\partial y} - \frac{\partial V}{\partial y}\Delta - 2\frac{\partial U}{\partial x}\frac{\partial^2}{\partial x^2} - \frac{\partial^2 V}{\partial y^2}\frac{\partial}{\partial y} + \frac{\partial^2 U}{\partial y^2}\frac{\partial}{\partial x}\right.\\
&\quad \left. - \frac{\partial^3 V}{\partial y^3} - 2\left(\frac{\partial^2 U}{\partial x\partial y}\frac{\partial}{\partial x} + \frac{\partial U}{\partial x}\frac{\partial^2}{\partial x\partial y}\right)\left(\frac{\partial^2}{\partial x^2} - \beta^2\right)^{-1}\frac{\partial^2}{\partial x\partial y}\right] - \sigma(x),\\
A_{12} &= 2i\beta\Delta^{-1}\left[\left(\frac{\partial^2 U}{\partial x\partial y}\frac{\partial}{\partial x} + \frac{\partial U}{\partial x}\frac{\partial^2}{\partial x\partial y}\right)\left(\frac{\partial^2}{\partial x^2} - \beta^2\right)^{-1}\right],\\
A_{21} &= -i\beta\frac{\partial U}{\partial y}, \qquad A_{22} = \frac{1}{Re}\Delta - U\frac{\partial}{\partial x} - V\frac{\partial}{\partial y} - \frac{\partial U}{\partial x} - \sigma(x),\\
B_{11} &= \Delta^{-1}\left(f\Delta + \frac{\partial f}{\partial y}\frac{\partial}{\partial y}\right), \qquad B_{22} = f, \qquad \Delta = \frac{\partial^2}{\partial x^2} + \frac{\partial^2}{\partial y^2} - \beta^2,\\
C_{11} &= \left(\frac{\partial^2}{\partial x^2} - \beta^2\right)^{-1}\frac{\partial^2}{\partial x\partial y}, \qquad C_{12} = -i\beta\left(\frac{\partial^2}{\partial x^2} - \beta^2\right)^{-1},\\
C_{31} &= i\beta\left(\frac{\partial^2}{\partial x^2} - \beta^2\right)^{-1}\frac{\partial}{\partial y}, \qquad C_{32} = \left(\frac{\partial^2}{\partial x^2} - \beta^2\right)^{-1}\frac{\partial}{\partial x}.
\end{aligned}
$$

Here, f is the shape function of input forcing, which limits the forcing region [17].

References

[1]Sayadi, T., Schmid, P., Nichols, J., and Moin, P., "Reduced-order representation of near-wall structures in the late transitional boundary layer," *J. Fluid Mech.*, Vol. 748, 2014, pp. 278–301.

[2]Schmid, P. and Henningson, D., *Stability and transition in shear flows*, Vol. 142, Springer Science & Business Media, 2012.

[3]Herbert, T., "Parabolized stability equations," *Special Course on Progress in Transition Modelling*, chap. 4, AGARD Rep., 1994, pp. 1–34, No. 793.

[4]Herbert, T., "Parabolized stability equations," *Annu. Rev. Fluid Mech.*, Vol. 29, No. 1, 1997, pp. 245–283.

[5]Ehrenstein, U. and Gallaire, F., "On two-dimensional temporal modes in spatially evolving open flows: the flat-plate boundary layer," *J. Fluid Mech.*, Vol. 536, 2005, pp. 209–218.

[6]Åkervik, E., Ehrenstein, U., Gallaire, F., and Henningson, D., "Global two-dimensional stability measures of the flat plate boundary-layer flow," *European Journal of Mechanics-B/Fluids*, Vol. 27, No. 5, 2008, pp. 501–513.

[7]Tumin, A., "Towards the foundation of global (bi-global) modes concept," *Global Flow Instability and Control-IV. Creta Maris, Hersonissos, Crete*, 2009.

[8]Chomaz, J., "Global instabilities in spatially developing flows: non-normality and nonlinearity," *Annu. Rev. Fluid Mech.*, Vol. 37, 2005, pp. 357–392.

[9]Nichols, J. W. and Lele, S. K., "Global modes and transient response of a cold supersonic jet," *J. Fluid Mech.*, Vol. 669, 2011, pp. 225–241.

[10]Mani, A., "Analysis and optimization of numerical sponge layers as a nonreflective boundary treatment," *J. Comput. Phys.*, Vol. 231, No. 2, 2012, pp. 704–716.

[11]Weideman, J. A. C. and Reddy, S. C., "A MATLAB Differentiation Matrix Suite," *ACM Trans. Math. Software*, Vol. 26, No. 4, December 2000, pp. 465–519.

[12]Alizard, F. and Robinet, J., "Spatially convective global modes in a boundary layer," *Physics of Fluids*, Vol. 19, No. 11, 2007, pp. 114105.

[13]Theofilis, V., "Advances in global linear instability analysis of nonparallel and three-dimensional flows," *Progress in aerospace sciences*, Vol. 39, No. 4, 2003, pp. 249–315.

[14]Theofilis, V., "Global linear instability," *Annu. Rev. Fluid Mech.*, Vol. 43, 2011, pp. 319–352.

[15]Monokrousos, A., Åkervik, E., Brandt, L., and Henningson, D. S., "Global three-dimensional optimal disturbances in the Blasius boundary-layer flow using time-steppers," *J. Fluid Mech.*, Vol. 650, 2010, pp. 181–214.

[16]Jovanović, M. R. and Bamieh, B., "Componentwise energy amplification in channel flows," *J. Fluid Mech.*, Vol. 534, July 2005, pp. 145–183.

[17]Ran, W., Zare, A., Hack, M. J. P., and Jovanović, M. R., "Low-complexity stochastic modeling of spatially-evolving flows," *Proceedings of the 2017 American Control Conference*, Seattle, WA, 2017, pp. 3815–3820.

[18]Bagheri, S., Henningson, D., Hoepffner, J., and Schmid, P., "Input-output analysis and control design applied to a linear model of spatially developing flows," *Applied Mechanics Reviews*, Vol. 62, No. 2, 2009, pp. 020803.

[19]Ran, W., Zare, A., Hack, M. J. P., and Jovanović, M. R., "Low-complexity stochastic modeling of spatially-evolving flows," *Proceedings of the 2016 Summer Program*, Center for Turbulence Research, Stanford University/NASA, 2016, pp. 285–294.